Appl Phys B (2012) 107:619–636
DOI 10.1007/s00340-012-4984-y

Applied Physics B
Lasers and Optics

Chemiluminescence as diagnostic tool in the development of gas turbines

F. Guethe · D. Guyot · G. Singla · N. Noiray · B. Schuermans

Received: 10 October 2011 / Revised version: 21 February 2012 / Published online: 26 May 2012

Abstract To optimise the operation of gas turbine combustors with respect to emission, cycle efficiency and components lifetime, increased attention has to be attributed to diagnostic techniques and more flexible control schemes. Chemiluminescence is an obvious choice and a relatively easy and low cost option for such a diagnostic tool. Application examples include spectral analysis and light intensity scaling, temporal analysis studying flame dynamic effects and imaging techniques resolving spatial distribution of heat release zones, as well as combinations of the methods like phase matched imaging and tracking of ignition kernels using high speed imaging. Further fundamental work should be triggered on the nature for the excited species and their formation pathways as well as their connection to heat release and the NO_x formation processes.

1 Introduction

In addition to fulfilling operational and fuel flexibility requirements, the design of gas turbine combustors is focussed on the optimisation of emissions (CO, NO_x), combustion stability (pulsations) and material lifetime. Therefore, the experimental observation and theoretical modelling of flames play a key role in gas turbine (GT) development. For the control and optimised operation of gas turbine combustion systems, respectively, the development of cost-effective and reliable sensor and diagnostic systems, which are effective over the whole operating range, is desired. The most relevant parameters for diagnostics purposes are flame or hot gas temperatures, since they determine the overall emissions, but from a practical point of view, a direct correlation to engine emissions would be sufficient. Especially for combustor homogenisation in annular premix combustors like the Alstom GTs this is a commercially available option [1].

While the NO_x formation depends approximately exponentially on flame temperature (T_{flame}) T_{flame} depends only linearly on the fuel fraction. Therefore the lowest NO_x are expected at fully homogenised combustor conditions. At real GT-conditions of an annular combustor inhomogeneities can derive from fuel distribution system, the air flow, off design seal or leakage effects in the combustor. To adjust such system to minimum NO_x a large potential is in the individual burner sensing and fuel flow control as described in [1].

Where optical access is limited. a passive method would be preferable over other optical or intrusive methods. Being relatively cheap to implement, chemiluminescence detection bears the potential for a feasible flame diagnostic. The chemiluminescence light emitted by the flame is well suited for diagnostic purposes since it carries the information about the local operation conditions. The chemiluminescence light is provided without external excitation and arises from excited species formed by the heat releasing reactions. The most important species in natural gas flames are OH^*, CH^* and possibly CO_2^*. While molecular temperatures can in principle be obtained by spectral fitting, the link to the corresponding equilibrium hot gas temperatures is not always justified. Also, the spectral fitting at elevated pressures and temperatures poses an experimental challenge as well as a theoretical one, since individual rotational lines are not discernible. It has been noted previously that the relative intensities of different species depend on the fuel equivalence ratios and show potential for a relatively simple sens-

F. Guethe (✉) · D. Guyot · G. Singla · N. Noiray · B. Schuermans
Alstom Power, Brown Boveri Strasse 7, 5401 Baden, Switzerland
e-mail: felix.guethe@power.alstom.com
Fax: +41-56-4665590

ing scheme. This approach has been successfully utilised in recording fast phenomena like thermo-acoustic pulsations and should be extended for operational control. This sensor development also benefits from theoretical and experimental kinetic studies. Several fundamental aspects concerning the origin and formation of the excited species await proper analysis.

While qualitative information about the flames temporal, spatial and spectral emission can be deduced relatively straightforward care has to be taken in the interpretation of the data especially trying to quantify them. Problems arise from chemiluminescence being line of sight technique and resulting uncertainties in their spatial occurrence and their link to heat release. Further the impact of turbulence, flame strain and curvature in technically relevant applications on the observable results makes the interpretation difficult especially for spatial imaging. This aspect is nicely studied and critically reviewed by Lauer and Sattelmayer [2–4].

The current paper summarises several aspects of applications of chemiluminescence sensing used in combustor development. Starting with some general remarks about optical flame spectra and filters, possible sensing strategies for burner optimisation are discussed including:

- Optical chemiluminescence spectra and filtered intensities to deduce the combustor status, i.e. the flame temperature, important for the emission of NO_x and CO (which itself depends on the equivalence ratio and inlet temperature as well as the composition of oxidiser (air) and fuel).
- Temporal variation to study dynamic and thermo-acoustic phenomena to optimise the combustors stability.
- Spatially resolved chemiluminescence images (line of sight integrated), which are used to monitor flame positions and their dependence on operating conditions to aid the optimisation of the burner concepts with respect to flame position, mixing quality, materials lifetime and to validate CFD models.
- The individual behaviour of ignition kernels can be visualised in high-speed imaging.
- Finally the combination of temporal and spatial variation is used to visualise mode shapes of thermo-acoustic instabilities, which can be compared to simulations and such information can be used to reduce instabilities in engine operation.

2 Flame chemiluminescence

Watching flames has been fascinating for people probably since humans were able to control and use it. To study the physics and chemistry of flames was an early trigger of scientific curiosity leading to several more or less valid concepts like phlogiston theory on one side or the foundations of modern spectroscopy on the other side. With modern scientific knowledge we currently understand the light emitted from flames (chemiluminescence) as a number of complicated exothermic physico-chemical processes that involve molecules in ground and excited states as well as their dynamics, kinetics and relaxation processes.

Observing the fire is still the first choice as a diagnostic tool for any flame in non-technical or technical context. While the nature of light emission of different flames ranges from atomic emission to particle and soot radiation a particularly promising kind of radiation is that from excited molecules. The most important species and spectra in flames have been previously described in the book of Gaydon [5]. For natural gas–air flames the most prominent species are the spectra of OH^* ($A\,^2\Sigma \rightarrow X\,^2\Pi$), CH^* ($A\,^2\Delta \rightarrow X\,^2\Sigma^-$) and C_2^* ($d\,^3\Pi_g \leftrightarrow a\,^3\Pi_u$). The nature of some broader bands has been noted and could be attributed to excited species of CO_2, CHO or CH_2O [6]. Since the nature of the carrier of that band is currently not unambiguously proven we will in this work refer to it as "broadband emission" and assume CO_2^* as the most likely candidate for the carrier. In practical flames the broad background is sometimes not even noted and appears to escape detection due to lack of structure, but nevertheless carries most of the light intensity. The use of well-calibrated instruments and careful reference spectra avoids these problems.

Only a further investigation allows us to link the information of the observable light to physical and chemical properties of the combustion and to explore the chemistry and physics of excited molecules as well as their relaxation process including fluorescence. Since the heat released in the flame by reaction of fuel with oxidants supplies sufficient energy the molecules are also formed in electronically excited states, which radiate in a fluorescence process. This process is called chemiluminescence and competes with radiationless transitions like collisions or competing reactions.

Little is known about the formation and further fate of excited species, especially on the molecular dynamics level. However the kinetic modelling of excited species has recently gained some more attention [7–10]. For natural gas flames the formation pathways are usually assumed to be

$$\mathrm{OH}(A \rightarrow X): \quad \mathrm{OH}^* \rightarrow \mathrm{OH} + h\nu$$

$$\mathrm{CH}(A \rightarrow X): \quad \mathrm{CH}^* \rightarrow \mathrm{CH} + h\nu$$

$$\text{Broadband emission} \quad \mathrm{CO} + \mathrm{O}(+M) \rightarrow \mathrm{CO}_2^* \rightarrow \mathrm{CO}_2 + h\nu$$

$$\text{unclear:} \quad \mathrm{CHO}^* \rightarrow \mathrm{CHO} + h\nu$$

$$\text{unclear:} \quad \mathrm{CH_2O}^* \rightarrow \mathrm{CH_2O} + h\nu$$

As pointed out before, a primary goal of the present study is a concept for a flame sensor to optimise technical flames with respect to their pollutant emissions. While such a sensing approach for a technical flame like a gas turbine combus-

tor can also use empirical correlations, some justifications for the methods should be given briefly.

The dominant parameter for NO_x ($NO+NO_2$) emissions in flames is the temperature and its temperature distribution in the combustor. The exponential behaviour of NO_x formation on NO_x is well known and has been described already over more than 60 years ago [11]. It is mainly based on reactions occurring mainly behind the original heat release zone. A more detailed view [12] splits the NO_x formation in a post flame and a prompt contribution with slightly different temperature scaling. The prompt NO_x formation is linked to the heat release according to "N_2O" [13, 14] and the "NNH" [15] pathways as well as the "Fenimore" [16] reaction of hydrocarbon intermediates.

Since all of these processes depend strongly on temperature, control of this quantity, respectively, its distribution has a priority in combustor development to improve the engine's overall emission behaviour.

3 Flame spectroscopy

3.1 Spectra and intensities

Naturally most fundamental studies on chemiluminescence have been undertaken under slightly idealised conditions at either atmospheric premixed or even laminar flames with standardised fuels and their validity under more realistic conditions has only recently received more attention [2, 17, 30]. From these standardised cases it can be deduced that in general the brighter flames have the hottest temperatures and also produce most NO_x.

In principle, the same is true for modern technical flames under partially mixed, highly turbulent conditions at elevated pressures. The spectra under high pressures are, however, more difficult to obtain and are more difficult to interpret as shown in Fig. 1. The optical access in a technical combustor that is part of a heavy duty power plant is a challenge, since transparent windows are not an option for commercial operation. Rather, optical probes with light guides or fibres extending several meters have to be used to detect the light. In the spectra, a large intensity of the black-body radiation is clearly visible in the red end of the spectrum, originating from hot structural parts of the combustor. The black-body radiation is increasing with T_{flame} and expected to be severe in GT applications. Especially the increased heat transfer from gas to combustor liner results in high background, which might not be observed in atmospheric experiments or externally cooled combustor walls. Furthermore, the relative intensity of the prominent peaks for high pressures is smaller than for the atmospheric flames. The broad background, usually assigned to CO_2^*, accounts for most of the chemiluminescence intensity in lean flames [18] and needs to be considered if CH^* or OH^* is to be investigated.

On the other hand it is clear that all chemiluminescence intensities are closely linked to heat release processes, since the excess energy to form excited species must come from exothermic reactions. Therefore the broad background can be taken as a whole to indicate the location of heat release as in imaging studies. An additional problem in technical applications under high pressure is the self-absorption feature of OH molecules, present in the combustor along the line of sight between the emitter and the detection optics, visible as a dip in the spectrum on the right side of Fig. 1. Since the emission of hot OH^* (formed in an exothermic reaction with non-thermal internal energy distribution) is broader and on a background of broadband emission, the actual peak near the origin of OH appears negative. This is due to colder ground state OH in the post flame zone (equilibrated to the hot gas temperature, but less energetic than the initially formed OH^*) between the emitting flame and the detection optics, which actually absorbs more light than is emitted by the OH^*. The CH^* feature does not exhibit this behaviour because the species occurs only in the real heat release zone and its concentration does not lead to significant absorption within the path of the chemiluminescence detection.

The rotational state distribution of the OH chemiluminescence spectrum around 307 nm can be fit but has shown not to be representative of the adiabatic flame temperature. It rather resembles as much a rotational state distribution corresponding to much hotter conditions [19, 20] not explainable by a Boltzmann type distribution law. This indicates that the emission takes place from an excited state,

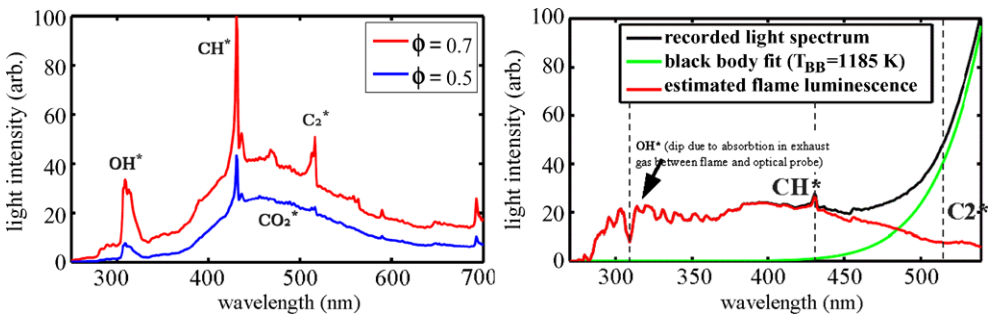

Fig. 1 Chemiluminescence spectra of swirl stabilised premix lab burners at atmospheric (*left*) and elevated gas turbine (>15 bar) pressure (*right*) [32]

which is formed in a "non-statistical" reaction yielding non-thermal product distributions but rather a distribution with preference for certain product states according to the nature of their transition state. A quantum dynamical explanation for this behaviour has, to the authors' knowledge, so far not been given. According to Gaydon [5] the reaction responsible for OH^* formation is $CH + O_2 \rightarrow CO + OH^*$. The CH^* spectrum around 431 nm however can be fit to product distributions that can be described by the Boltzmann law and seems to represent lower temperatures near the adiabatic flame temperature [21]. CH^* is either formed in a reaction yielding statistically thermalised products or the product states are thermalised sufficiently fast before they fluoresce (seen as chemiluminescence). This makes in the CH^* feature around 431 nm in principle a good candidate for sensor indicating flame temperature.

On the other hand this makes OH^* alone a not a good candidate for a robust sensing strategy but rather another band or combination of bands pass filters should be chosen. The effects of view angle variation and optical contamination resulting in changes of the total intensity lead to a sensing strategy that allows one to use a relative measure like the relative band intensity of two or more optical filters or a spectral fit to certain spectral features.

3.2 Flame sensing

The use of chemiluminescence for flame sensing purposes has been demonstrated before by several groups [22–26]. The industrial application for gas turbines has been demonstrated for Alstom GT13 [1]. The difference in scaling of the intensity of the different chemiluminescence emission bands was noted previously [27, 28], and an equivalence ratio (ϕ) sensing scheme was proposed. In particular the varying slope with ϕ of the intensity of the bands around 310 nm and the one at around 431 nm, usually attributed to excited states of OH and CH, made the ratio of the two bands (OH^*/CH^*) a good candidate for a flame sensor.

For perfectly premixed flames the chemiluminescence intensity (I) depends linearly on the mass flow rate m_{air} and exponentially on ϕ and pressure p. In the case of a globally uniform equivalence ratio distribution the following fitting ansatz for that species was chosen as explained in Guyot et al. [26]:

$$I = k m_{\text{air}} \phi^{\beta} p^{\gamma} \tag{1}$$

Here k is a constant for one chemical species accumulating their optical and chemical specifics and β and γ are exponents. Typical values for β are 4 ± 2. The pressure coefficient γ was given by Higgins [27, 28] to be -0.86 for OH^* and -0.64 for CH^*. The non-integer polynomial fit has been chosen for historical reasons, although most likely a more exponential or Arrhenius type behaviour is to be expected since the excited species are formed by chemical reactions following Arrhenius type reaction rates [30]. For the current approach, however, only the difference in slope in a relatively small range of different species is relevant. In terms of T_{flame}, an exponential fit like (2) also is also useful. We have

$$I = I_0 \cdot e^{T \cdot B_I} \tag{2}$$

with B_I as exponential factor and I_0 as pre-exponential factor. A fundamentally more accurate description would be much more complicated. The fit should be done either on temperature (assuming a constant inlet temperature) or on equivalence ratio ϕ but not on both in the same expression. In this case, for fitting this relatively small range, and for simplicity this exponential function is taken to be sufficient. In consequence, the ratio of two different intensity signals (i.e. CH^*/OH^*) is a function of the equivalence ratio only. After calibration measurements, the CH^*/OH^* ratio provides a measure of the equivalence ratio [27]:

$$\frac{I_{\text{CH}^*}}{I_{\text{OH}^*}} = \frac{k_{\text{CH}^*}}{k_{\text{OH}^*}} \phi^{(\beta_{\text{CH}^*} - \beta_{\text{OH}^*})} \tag{3}$$

In combustion experiments the NO_x concentration at the combustor exit is often described by an exponential fit to emission data (more precisely often Arrhenius type exponential functions are formulated [29]):

$$[\text{NO}_x] = [\text{NO}_{x_0}] \cdot e^{T \cdot B_{\text{NO}_x}} \tag{4}$$

With B_{NO_x} as exponential factor and NO_{x_0} as pre-exponential factor. T represents the temperature of the heat release zone. Since the light intensity can be approximately described as scaling exponentially with T_{flame} similar to NO_x formation (4), it is reasonable to consider a direct link between the hot regions of a combustor to the NO_x forming regions.

In particular the formation of "prompt" NO_x, usually formulated through species like from CH ("Fenimore"), requires energetic species with high internal energies helping to overcome the high activation energy required for breaking of the stable N–N triple bond that makes molecular nitrogen so stable (allowing combustion to operate at low NO_x-emissions far from equilibrium NO_x levels of several 1000 ppm). Candidates for such reactions should also include hot excited states (electronically and rovibrationally) of OH^* or CH^*, as discussed here for optical emission. Their lifetimes are limited by emission and collisional quenching (mostly with N_2 molecules). The collisions with N_2 can, however, also yield reaction products as they are formulated for "prompt" NO_x formation. Although the relative abundance of excited species is orders of magnitude below that of formed NO_x at any given time it has to be considered that the NO_x once formed remains throughout the combustor while the excited concentration decays fast. Since their

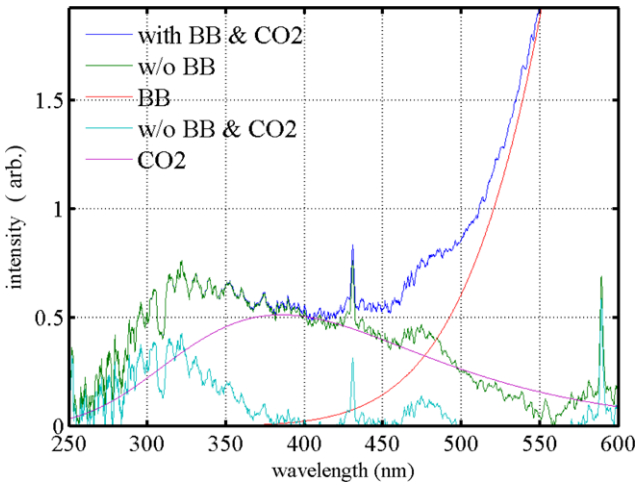

Fig. 2 Chemiluminescence spectrum of sequential combustion flame at engine scale burner and pressure conditions (>10 bar) in lean conditions

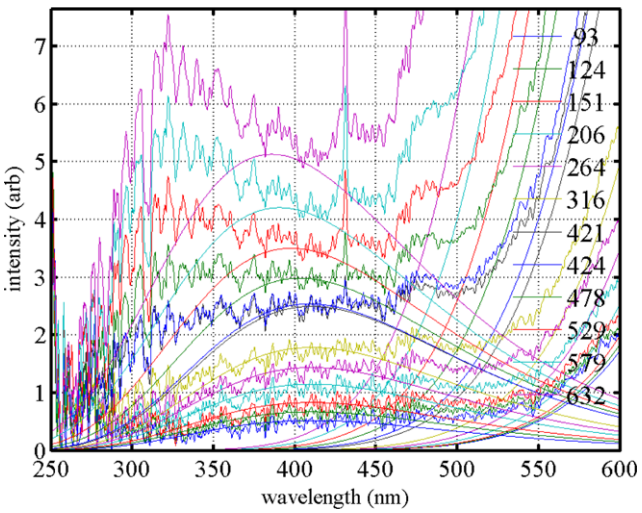

Fig. 3 Chemiluminescence spectra for varying flame temperatures (expressed as ΔT_{flame}) for constant $T_{\text{SEV\_in}}$ at engine scale burner and pressure conditions. Also shown are the fitted black-body radiation and the broadband emission background

formation pathways lead back to the fuel in a long series of reactions the overall probability of excited species formation from fuel is comparable to that of NO_x formation. The high excess energy of these species and their ability to react with N_2 make this a possible alternative formulation of the prompt formation pathway or at least an additional path. From this it can therefore be rationalised that the brightest burners are also producing most NO_x-emissions, which gives a good concept for an optimisation strategy. Furthermore, the chemiluminescence reveals details about the nature of the flame chemistry and physics. The importance of chemiluminescence research from idealised kinetic experiments to large scale applied detection does not only help to understand NO_x formation, but it can also yield insight into the timescales of formation, which are probably closely linked to the kinetically description of ground state chemistry [30].

In technical combustors the optical access is usually very limited and the view angle has a strong influence on the recorded spectra. If for example the flame is viewed from down stream through a zone of hot exhaust gas the ground state OH population (near T_{hotgas}) is relatively high and leads to absorption features near the band origin (visible in spectra Figs. 1, 2 and 3), which can lead to a prominent absorption peak, seen as dip rather than an emission peak. The emissions of the electronically excited species, which are also rovibrationally hot, are then detectable only through their hot bands at lower and higher wavelengths compared to the band head.

In order to approach a GT engine application this procedure is being validated in more and more realistic conditions in terms of turbulence, flow field and pressure as well as operation in the a secondary combustor operating at autoigniting conditions [31]. As an important step towards GT application the previously presented demonstration [26] of chemiluminescence sensing for a premixed swirl-stabilised flame under atmospheric conditions was very promising. However, the introduction of turbulence and the occurrence of recirculation zones, common in technical combustion systems, made the straightforward interpretation of the two photomultipliers' signal difficult, since a strong and broad background contributes to the signal at least on the CH^* channel. A correction for that background contribution to the CH^* peak utilising a third photomultiplier similar to the method described in [22] could improve the relation significantly.

Validation of the multiple band photo multiplier technique in connection with siren excitation has been used to derive the flame transfer functions (FTF) under pressure [32] in a full-scale burner test rig. In continuation of the work, studies on the reheat combustor (sequential environmental burner—SEV) are a logical next step to extend the methodology for GT-applications. A spectrum recorded at the high pressure rig is shown in Fig. 2. The spectra were obtained at an Alstom full scale test rig running at full engine pressure at the DLR Cologne facilities on a prototype engine reheat burner. The reheat test rig has also been described in [33]. The view direction is upstream of the combustor through a wide-angle lens covering almost all of the flame extension through the hot gas near the emissions probe. The view port is usually used for flame supervision by standard video (or optionally also intensified) cameras and consists of a water-cooled optical probe protruding in the hot gas flow.

3.2.1 Spectral decomposition

Light is collected through a sapphire window by a lens and is than lead from the rig via a 20 m long UV transparent optical fibre to the control room where the light was split onto several photomultipliers and a spectrometer in the visible and UV range (USB4000-UV-VIS from Ocean optics). Per measurement point 10 spectra with of 1 s integration time were averaged. This allowed the recording of spectra for further analysis and the direct recording of photomultiplier signals for fast and time dependent detection simultaneously. The spectral resolution (∼1.5 nm), obtained with the used instrument, is sufficient to resolve the broad band structure required to determine a sensing strategy based on filters. However, it is probably not sufficient for reliable fits of rotational envelopes.

As a first step the recorded (raw) spectra have to be corrected for dark current of the detection array, transmission of the optical elements and the detector sensitivity. The correct calibration of the spectral intensities over a wide range (i.e. 250 and 900 nm) is crucial for the understanding of the spectrum and the following analysis. An example for such a spectrum is shown as a blue line in Fig. 2 (from 250–600 nm). It resembles the actual light, as it is detectable by any instrument (spectrometer, camera or spatially integrated photo sensor). Most intensity stems not from the flame, but from the black-body radiation (shown in red) of the hot combustor, which is in the background of the view field. This part dominates the spectrum in the red part and can be fit a by the well-known Planck formula (5) based on regions with minimum interference from optical transmission curves and reveals an averaged combustor wall temperature (actually probably closer to the maximum combustor wall temperature in the line of sight). We have

$$I_{\mathrm{BB}}(\lambda, T_{\mathrm{BB}}) = A \cdot \frac{2hc}{\lambda^5} \cdot \left(e^{\frac{hc}{\lambda \cdot k T_{\mathrm{BB}}}} - 1\right)^{-1} \tag{5}$$

with I_{BB} = black-body intensity, λ = wavelength, h = Planck's constant, k = Boltzmann constant, c = speed of light, T_{BB} = black-body temperature, A = scaling constant. The fit works relatively well using only two fitting constants A and T_{BB} if the λ-region is properly selected to exclude any irregularities in the transmissions spectra of the optical setup like i.e. absorption features of the silica fibre. The obtained temperatures scale very well with thermocouple measurements on the combustor walls and could be used so as to do surface temperature measurements in the context of heat transfer studies.

The remaining spectrum can be interpreted as stemming from the flame resembling the actual chemiluminescence shown in green and is dominated by broad background (already described in [18, 23]) with the known features of OH* and CH* as discussed earlier. It is important to note that the prominent features known from laboratory flames seem not to be dominant anymore at GT conditions in terms of overall intensity or spectral significance. Also visible is a broad feature on the shoulder of the black-body radiation around 470 nm, which currently cannot be assigned. The large width and the absence of a C_2^*-origin (around 516 nm) makes the explanation as C_2^* hot band unlikely and cannot serve as explanation of this feature.

A further step in the decomposition of the spectrum is the attempt to fit the broadband emission background as described in [26] to formula (6) given by Brockhinke et al. [34] for low pressure flames:

$$I_{\mathrm{CO}_2^*}(\lambda, T_{\mathrm{BB}}) = A \cdot e^{\left(-e^{\left(\frac{-(\lambda-\lambda_c)}{w}\right)} - \frac{\lambda-\lambda_c}{w} + 1\right)} \tag{6}$$

with $I_{\mathrm{CO}_2^*}$ = intensity of the broadband emission background (tentatively assigned to CO_2^* by the authors [34]), λ_c = wavelength of maximum intensity, A = scaling constant, and w for the width of the peak. The fit was used to isolate the known molecular band around 431 nm and 310 nm and separate them from the assumed broadband emission. Therefore, the fit was performed to match the intensities at 400 nm and 450 nm leaving the 431 nm feature visible and the 310 nm also in reasonable band shape. The fitting was done varying λ_c, A and w. The width w had to be restricted to a maximum of 80 nm to avoid the overlap with the molecular band of OH* extending in blue part of band. The peak maxima are then around 400 nm and leave a residual spectrum consisting of only molecular bands, as they are well known from atmospheric flames. It is somewhat unsatisfactory that a physical explanation for this fit is missing, but the very good correspondence to the observed spectra from low pressure to high pressures over the whole range of conditions tested in this work is striking. Therefore the fit was used in subsequent processing only for comparison and further studies concerning this observation are encouraged. The following simulations of band intensities are however done without the subtraction of the black body and broadband to resemble GT conditions.

3.2.2 Band pass filtered intensities

SEV spectra for varying flame temperatures are given in Fig. 3. The change of the emission spectrum with temperature towards the UV can clearly be seen. The flame temperature is given as the difference between SEV flame and inlet temperature, $\Delta T_{\mathrm{flame}} = T_{\mathrm{flame}} - T_{\mathrm{SEV\_in}}$. The distinct spectral patterns including molecular bands, hot bands and broad features, are present over the whole range in all spectra and are exactly repeated for all conditions indicating their nature as true (but unassigned) features rather than experimental artefacts. For low temperatures (at lean conditions) the CH* and OH* bands seem to disappear completely. Nevertheless a suitable choice of filters should allow reproducing

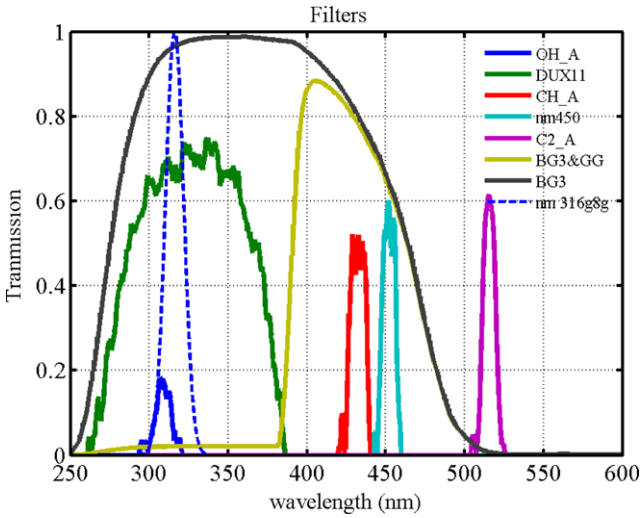

Fig. 4 Collection of filters and filter combinations to study the multiple band detection schemes. Shown are measured transmission spectra when, available, supplier data for BG3 and (BG3 & GG395 nm) or simulated data for 316g8g

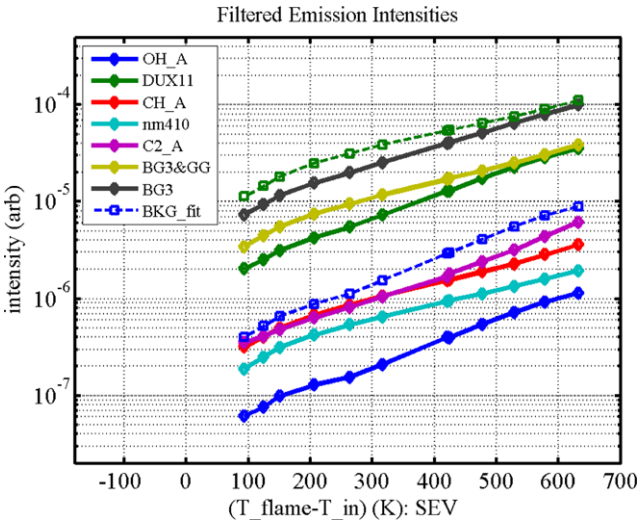

Fig. 5 Intensity of filtered chemiluminescence intensities calculated from the spectra from Fig. 3 vs. ΔT_{flame}

this temperature scaling from relative intensities also on the broadband features. For this either the time averaged photomultiplier signals could be used directly or the simulated intensities from the measured spectra, as a sensor would detect it (including black-body and broadband emission background radiation), respectively, their ratio for any given filter combination can be used to derive a sensing concept.

The ideal filter has to minimise the impact of the black-body radiation and be broad enough to capture the OH* radiation with minimal impact of the narrow absorption feature. A possible strategy would be to use separate filters for the UV part of the spectrum below 350 nm and one for the visible part of over 400 nm. Preferred filters would be readily available low cost colour glasses with wide opening ranges rather than expansive narrow band dichroic band filters. The band intensities were simulated from measured spectra with the filter functions as shown in Fig. 4. The filters of choice were: a narrow band (fwhm 10 nm) OH* filter (near the origin) centred around 307 nm, a UG11 colour glass filter with dichroic coating (DUX 11), a CH* filter around 431 nm, narrow band pass filters around 450 nm (for the broad background) and 516 nm (C_2^*), as well as a BG3 colour glass without and in combination with a GG395 nm cut off filter. For the numerical simulations it is also possible to custom design any filter like a filter of central wavelength 316 nm with a Gaussian profile of 8 nm width. This filter is chosen to minimise the effect of self-absorption of the colder OH (at T_{hotgas}) near the origin of 307 nm and still represent OH* emission using their hot band emission.

The change of intensities in the different bands is shown in Fig. 5 on logarithmic scale. These values were derived by convoluting the experimental spectra from Fig. 3 and the filter from Fig. 4. All intensities are monotonously increasing with T_{flame} and therefore would be suitable as flame sensors. The intensity of the narrow band filters is lower than that of the colour glasses with BG3 transmitting most light. For comparison, the intensity according to the fit of the broadband emission background is also plotted. To be independent of optical degradation, aging or dirt congestion the ratio of two signals would give a much more robust signal if that ratio is dependent on T_{flame}, since both signals would approximately be affected in the same way leaving the ratio of signals constant. For this, the difference in slope needs to be considered. Figure 5 shows a different slope with T_{flame} for the BG3 filter variants and the broadband emission background fit. The "C_2^*" filter (∼526 nm) is farthest to the red and is clearly responding to increased combustor wall temperature contribution to the signal by a steeper increase. The signals of the filter around 431 nm and 450 seem to be almost parallel indicating that the main contribution is from the broad background common to both signals and the CH* band is negligible. The earlier mentioned [22, 26] correction of the CH* band by subtracting the estimated background contribution from a spectral region nearby but without molecular features has been proposed has been carried out with the current data. The method has however not been proven useful since the results exhibit a large scatter and therefore do not improve the procedure. The attempts are therefore not shown here. At least it has to be ruled out for a robust sensing concept.

The ratios of several filter intensities from Fig. 5 are plotted in Fig. 6. As already visible from the spectra in Fig. 3 most ratios are not sensitive in the low temperature regions, which is limiting the applicability of this method. However, a clear trend is visible at intermediate temperatures when the main part of the flame spectrum has moved in the UV region and the relative changes become small. The ratio of highest

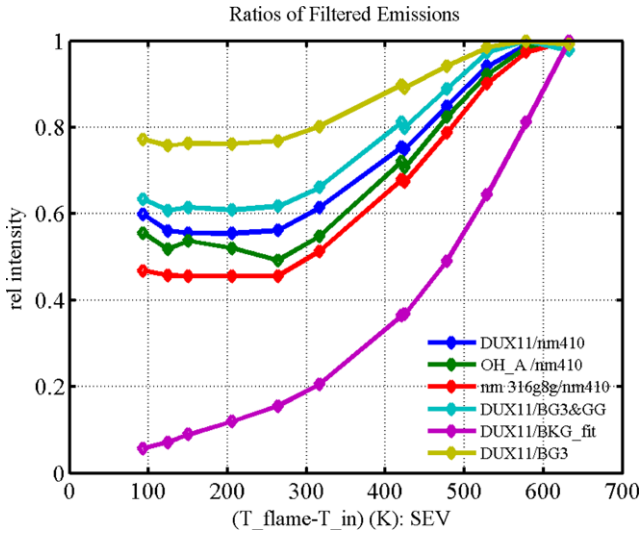

Fig. 6 Ratios of filtered intensities of Fig. 5 scaled to a scale of 0 to 1

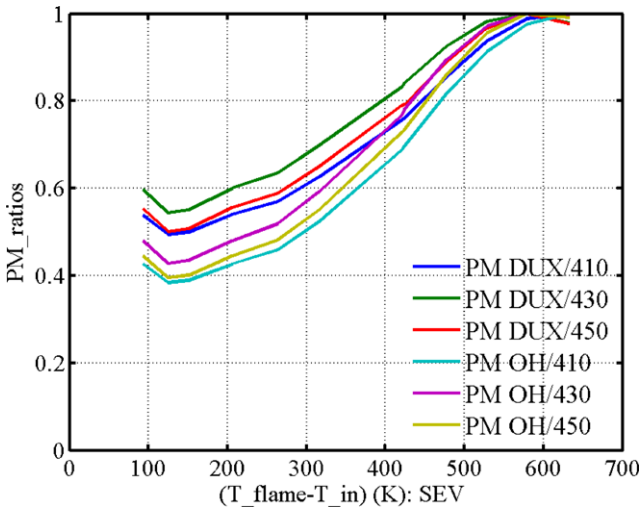

Fig. 7 Ratios of time averaged measured photo multiplier intensities like Fig. 6 scaled to a scale of 0 to 1

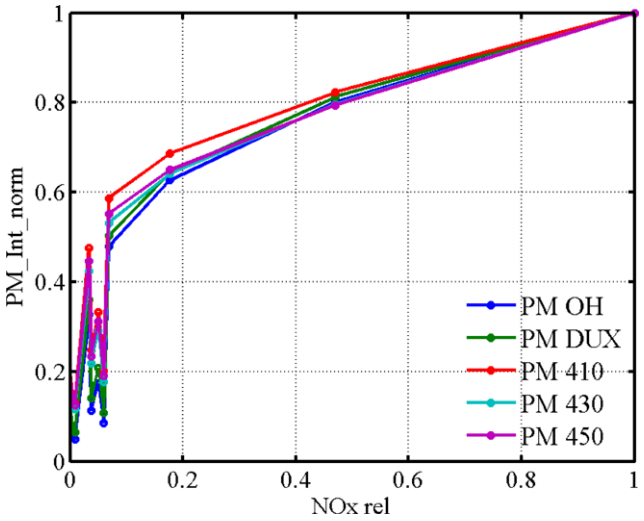

Fig. 8 Time averaged measured photo multiplier intensities. Same data as in Fig. 7 plotted vs. NO_x (normalised to maximum)

sensitivity among the band filters seems to be the simulated filter around 316 nm (slightly red of the OH^*-origin) with respect to the centre of the broadband peak at 410 nm.

Interestingly the intensity of the broadband emission background as simulated with (6) seems to be a very useful property since the ratio to DUX 11 filter is changing monotonically over the whole range of T_{flame}. Although the values were obtained strictly experimentally by modelling the spectra in the described manner it was not possible to design a filter that could reproduce this behaviour exactly in a single photo multiplier reading. Such a filter or combination of filters would be most useful. These findings highlight once more the importance of this broad emission band and should encourage further work to clarify the nature of this band.

Several filter combinations recorded with photomultipliers directly (time averaged over 20 s) are shown in Fig. 7 and exhibit a similar picture as in Fig. 6 for the filter ratios proving the technical feasibility of this approach also without operating a spectrometer.

The direct link of photomultiplier intensities to NO_x emissions is demonstrated in Fig. 8 where they are plotted vs. normalised emission values. Below a certain threshold of low T_{flame} and correspondingly low emissions and large measurements errors all intensity graphs increase monotonically with emissions indicating their potential to identify high emission burner flames.

A corresponding plot for the simulated filter ratios (being more robust towards optical alignment and dirt problems) is shown in Fig. 9. Again all ratios increase slightly with NO_x emissions with the ratio of the DUX 11 filter to the (synthetic) broadband emission background showing the largest dynamic range.

The monotonic behaviour of NO_x formation and light intensity for NO_x values of significant magnitude could resemble the fact that both processes follow trends that can be fit exponentially. Their relationship can in principle be related to kinetically derived expressions. This observation is to be expected and can be taken to justify the application of chemiluminescence sensing for NO_x reduction.

As mentioned previously, the occurrence of excited state molecules (in chemiluminescence) with excess energies sufficient to overcome the high activation energy stabilising the N_2 molecule and the formation of (at least) "prompt" NO_x are somehow linked. The role of excited species in prompt NO_x formation is however speculative and would require more fundamental work on theoretical and molecular dynamics side.

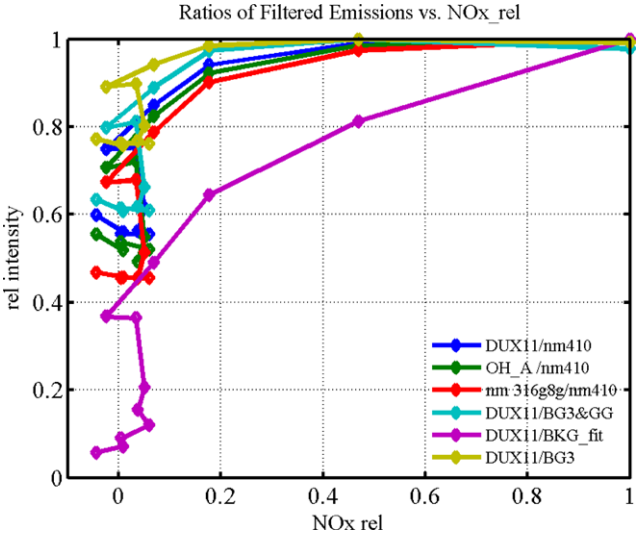

Fig. 9 Same data as in Fig. 6 plotted vs. NO_x (normalised to maximum) and CO vs. NO_x emissions (normalised to maximum) emissions

The data presented in this section reveal some difficulties in the interpretation of chemiluminescence and their link to heat release. If properly measured their integrated intensity is however monotonically dependent on heat release and therefore the use as indicator of heat release fluctuations and spatial distributions is at least for qualitative interpretations justified.

4 Chemiluminescence and temporal of heat release fluctuations

Another integrated part in Alstom's gas turbine technology and product development process, to which chemiluminescence detection is contributing, is the thermo-acoustic assessment of gas turbine combustors. The approach to thermo-acoustic analysis is to use measured flame transfer functions in an acoustic network model, which simulates the acoustic wave propagation through combustion chamber. A crucial aspect of this modelling approach is to obtain a correct representation of the interaction between the heat release and the acoustic field in the combustor.

Flame transfer functions are measured in a single burner test facility and models are fitted to this transfer function data in order to predicting the thermo-acoustic operational behaviour of multi-burner gas turbine combustion systems. Equation (7) shows the link between the systems acoustic field and the heat release at the heat source (i.e. the flame):

$$\begin{aligned}\frac{\hat{u}_\mathrm{h}}{\hat{u}_\mathrm{c}} &= 1+\left(\frac{T_\mathrm{h}}{T_\mathrm{c}}-1\right)\frac{\bar{u}_\mathrm{c}}{\hat{u}_\mathrm{c}}\frac{\hat{Q}}{\bar{Q}}\\ &= 1+\left(\frac{T_\mathrm{h}}{T_\mathrm{c}}-1\right)\mathrm{FTF}(\omega)\end{aligned} \tag{7}$$

where Q is heat release, u is velocity, T is temperature and $\mathrm{FTF}(\omega)$ is the frequency dependent flame transfer function. Subscript c indicates "before flame (cold)", subscript h indicates "after flame (hot)", $(\bar{\cdot})$ indicates a quantity's mean part and $(\hat{\cdot})$ and indicates its Fourier transform.

Triggered by the limited access in an industrial high-pressure test facility, Alstom has developed a technique to obtain transfer functions from only three pulsation probes and multiple chemiluminescence sensors. The chemiluminescence intensity signals are used as a measure for the flame's heat release.

Using chemiluminescence signals to combustion system's heat release is not very straight forward, because heat release fluctuations may be caused by fluctuations of the fuel to air ratio, fluctuations of the mass flow, or a combination of both.

This is expressed in

$$\begin{aligned}Q = m_\mathrm{fuel}H_\mathrm{fuel} &= m_\mathrm{air}\phi\left(\frac{m_\mathrm{fuel}}{m_\mathrm{air}}\right)_\mathrm{stoich}H_\mathrm{fuel}\\ &\xrightarrow{\text{linearisation}} \quad \frac{Q'}{\bar{Q}} = \left(\frac{m'_\mathrm{air}}{m_\mathrm{air}}+\frac{\phi'}{\bar{\phi}}\right)\end{aligned} \tag{8}$$

where Q is equivalence ratio, m is mass flow entering the reaction zone (= flame area × burning velocity × density), H is chemical enthalpy. The subscript stoich indicates stoichiometric conditions and $(\cdot)'$ indicates a quantity's fluctuating part. Equation (1) indicates that the chemiluminescence intensity is not necessarily proportional to the heat release. To be able to utilise the flames chemiluminescence for the thermo-acoustic approach, detection on different wavelengths bands was used. We assume that the intensity of the nth optical signal shows the following dependence on mass flow and equivalence ratio (following (1) and (3)):

$$\begin{aligned}I_n &= k_n m_\mathrm{air}\phi^{\alpha_n}\\ &\xrightarrow{\text{linearisation}} \quad \frac{I'_n}{\bar{I}_n} = \left(\frac{m'_\mathrm{air}}{m_\mathrm{air}}+\alpha_n\frac{\phi'}{\bar{\phi}}\right)\end{aligned} \tag{9}$$

where k_n and α_n are constants for one chemical species, e.g. OH^*, which can be determined in steady calibration measurements (no excitation), in which m and ϕ are varied. For N optical signals this can be written in matrix form. If $\alpha_i \neq \alpha_j$, the system can be inverted in a least square sense, in order to calculate $\frac{m'_\mathrm{air}}{m_\mathrm{air}}$ and $\frac{\phi'}{\bar{\phi}}$ from measured $\frac{I'_n}{\bar{I}_n}$ during excitation:

$$\begin{pmatrix}\frac{I'_1}{\bar{I}_1}\\ \vdots\\ \frac{I'_N}{\bar{I}_N}\end{pmatrix} = \begin{bmatrix}1 & \alpha_1\\ \vdots & \vdots\\ 1 & \alpha_N\end{bmatrix}\begin{pmatrix}\frac{m'_\mathrm{air}}{m_\mathrm{air}}\\ \frac{\phi'}{\bar{\phi}}\end{pmatrix} \tag{10}$$

$$\xrightarrow{\text{Pseudo-inversion}} \quad \begin{pmatrix} \frac{m'_{\text{air}}}{\bar{m}_{\text{air}}} \\ \vdots \\ \frac{\phi'}{\bar{\phi}} \end{pmatrix} = \text{pinv}\left(\begin{bmatrix} 1 & \alpha_1 \\ \vdots & \vdots \\ 1 & \alpha_N \end{bmatrix} \right) \begin{pmatrix} \frac{I'_1}{\bar{I}_1} \\ \vdots \\ \frac{I'_N}{\bar{I}_N} \end{pmatrix}$$

Now the flame transfer function can be determined, provided $\frac{\bar{u}_c}{\hat{u}_c}$ is known, e.g. from acoustic measurements as done in this work:

$$\text{FTF}(\omega) = \frac{\bar{u}_c}{\hat{u}_c}\frac{\hat{Q}}{\bar{Q}} = \frac{\bar{u}_c}{\hat{u}_c}\left(\frac{m'_{\text{air}}}{m_{\text{air}}} + \frac{\phi'}{\bar{\phi}}\right) \tag{11}$$

The described technique has been validated at atmospheric and elevated pressure and is discussed in detail in [32, 35]. At high pressure the correct measurement of the flame chemiluminescence is more challenging than at atmospheric conditions. This is due to constrains regarding optical access to the flame, an overlapping of the wavelengths bands of flame luminescence and the combustor walls' heat radiation and the generally lower probability of the formation of the chemical species associated to the flame chemiluminescence under high pressures.

The graph on the right side of Fig. 1 shows an example of a light spectrum recorded at high pressure during a transfer function measurement campaign. In Fig. 10 the optical technique to determine flame transfer functions is compared to an alternative technique that uses only pulsation probe signals. Both methods are in good agreement.

Being able to measure transfer functions at high pressure conditions on full scale burners opens up the possibility to predict thermo-acoustic behaviour of gas turbines using different fuels such as natural gases with higher hydro-carbon content, syngases and liquid fuels, whose combustion properties depend on pressure differently.

5 Spatial distributions

5.1 High pressure imaging

A further chemiluminescence technique frequently used is the analysis of their spatial distribution by mean of imaging techniques using intensifiers or just standard video imaging. With the use of appropriate filters and filter combinations it is possible to visualise the flame position for varying operating conditions and their temporal fluctuations. An example is shown in Fig. 11 on an atmospheric SEV test rig. More details about the rig can be found in [36]. The atmospheric rig has large quartz windows and allows a better view on the flame directly (without using fibre optics or endoscopes). For the intensified UV sensitive camera 3 different band pass filters at 308 nm (OH^*), 430 nm (CH^* and background) and 450 nm (background) were used. All images show the flame at identical conditions. The upper image indicates the flow direction perpendicular to the line of sight in a single snap shot without filter. The lower three images are filtered as indicated averaged over 300 images. The different flame position at identical heat release positions reveal that the different species are also formed at different locations corresponding to different times in the heat release process with CH^* being formed the earliest followed by OH^* and the background chemiluminescence recorded at 450 nm. In the right plot in Fig. 11 the image filtered around 450 nm has been subtracted (after normalisation) from the image filtered around 308 nm (the expected OH^* peak) to visualise their relative difference in location. The difference indicates a red region where the relative intensity of the OH^* is higher than for the background at 450 nm. This observation would support the assignment of $CO + O \rightarrow CO_2^*$ as source of the chemiluminescence as being late in the combustor when CO has already been formed while CH^* and OH are in the early heat release zones.

Under high-pressure conditions spatial imaging becomes more demanding since the optical access is limited and large gals windows are no longer an option. The use of optical fibroscopes is necessary in connection to intensified cameras to be able to detect enough light intensity for filtered heat release imaging. With the appropriate set up of hard and software even correlations to pulsation signals and phase angle resolved detection is possible.

As briefly explained already in [33] images were taken at the high pressure test cell at DLR Cologne at full scale GT burners with an UV transparent fibroscope filtered with DUX 11 filter. The light was detected on an intensified camera with variable opening times between 20 µs to be able to detect fast phenomena in the kHz order up to −800 µs for good light averaging. The original image is recorded, background-subtracted and rotated to compensate for the distortion caused by the fibre. The view field shows approximately the first third of the combustor and the flow direction

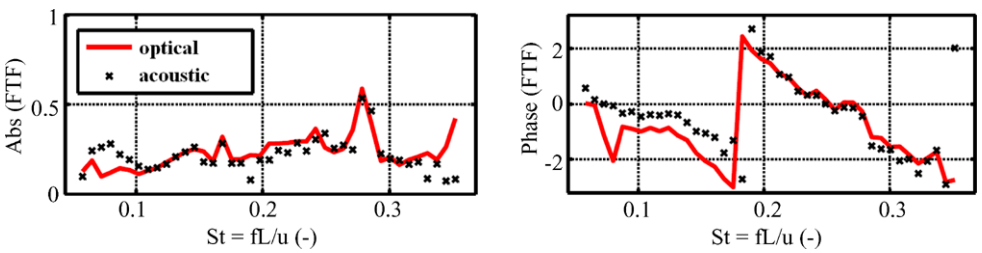

Fig. 10 High-pressure transfer functions obtained from optical data show good agreement with transfer functions obtained from a purely acoustic method

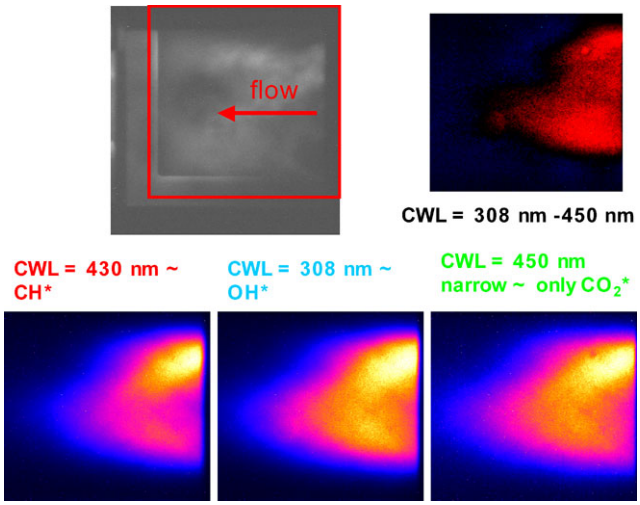

Fig. 11 Atmospheric SEV flame observed without filters (*upper image*: single shot, flow from left to right) and with filters as indicated (*bottom graphs*) in side view perpendicular to the flow. The difference of the normalised graphs in the *upper right corner* exhibits higher intensities (*red*) of the 308 nm band upstream than for the 450 nm

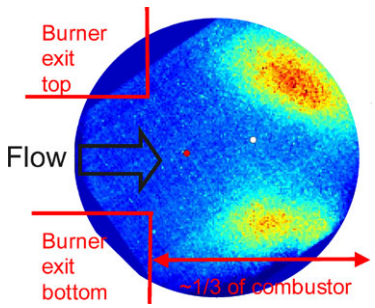

Fig. 12 SEV- chemiluminescence image recorded at full pressure conditions with UV fibroscope and DUX 11 filter (taken from [33]) at side view perpendicular to the flow

is indicated in Fig. 12. Note that the CCD chip is mounted in a diagonal angle to the flow direction revealing region of zero intensity (in blue). Since the optics are located in a very small area of few mm with a wide opening angle the line of sight integration by the chemiluminescence makes the interpretation less obvious than observation through a window or even 2D laser sheet methods. The comparison of different images however gives a clear indication of variation in the flame.

These images can be used to visualise the flame and observe flame position and shape in dependence of operating parameters. In Fig. 13 this is shown for varying fuels and varying air composition simulating flue gas recirculation. Clearly with increasing FGR and decreasing O_2 the flame reactivity is reduced and the flame moves further down stream. For lowest reactivities most of the flame appears to be down stream and out of the view field. Since the SEV flame is dominated by the auto-ignition the flame position is highly dependent not only on O_2 but also on the fuel compositions expressed as the sum of higher hydrocarbons in natural gas (C_2^+ content). The least reactive condition corresponding to the flame farthest downstream is high FGR and pure CH_4 flame in the lower left corner of Fig. 13 while the most reactive condition are found at no FGR and 18 % C_2^+ where the flame is located in two lobes in the centre of the view field stabilised by the ignition point only. Nevertheless, all shown images refer to stable combustor operation points of this sequential burner.

The flame is only slightly moving downstream when O_2 at the inlet is reduced indicating that flame stabilisation other than a pure auto-ignition mechanisms is also actively keeping the flame lit. This is also supported by the observation that the low reactivity flames appears to move not only downstream, but also towards the outer regions away from the centre line.

For the higher C_2^+ values the flame is clearly following the trend of higher reactivity with C_2^+ and with O_2 content by moving upstream towards the combustor according to a reduction in ignition time.

5.2 High speed imaging and ignition kernel tracking

Unlike the more common premix combustion, which is dominated by the physics of flame propagation the combustion mechanism of the sequential combustor is based on auto-ignition occurring spontaneously without flame propagation being required. The ignition delay time and the flow velocity are the dominating factors determining the flame location within the combustion chamber. With the optical access to the high pressure rig given as described the use of an intensified camera allows to record consecutive images with 100 µs (or less) shutter time. With a high speed system it is possible to follow the kernels of such ignition processes through the combustor at a sampling rate of 10 kHz. Results are presented in Fig. 14. In the following discussion a single combusting hot gas pocket is called ignition kernel. The importance of ignition kernels for combustion in the auto-ignition regime in turbulent flame has been addressed very nicely by Mastorakos [37] and others [38]. A kernel, once spontaneously ignited, is also subject to flame propagation and transport driven processes since the occurrence of heat release is time dependent. The kernels can, after ignition, be viewed as flowing igniters in a turbulent combustion environment. The occurrence and the travelling speed of this structures is important in the understanding of the sequential combustion physics.

The steps followed in identification and tracking of kernels may be summarised as follows:

1. The upper and lower regions of the view field are considered separately to improve kernel identification in varying levels of average flame intensity.

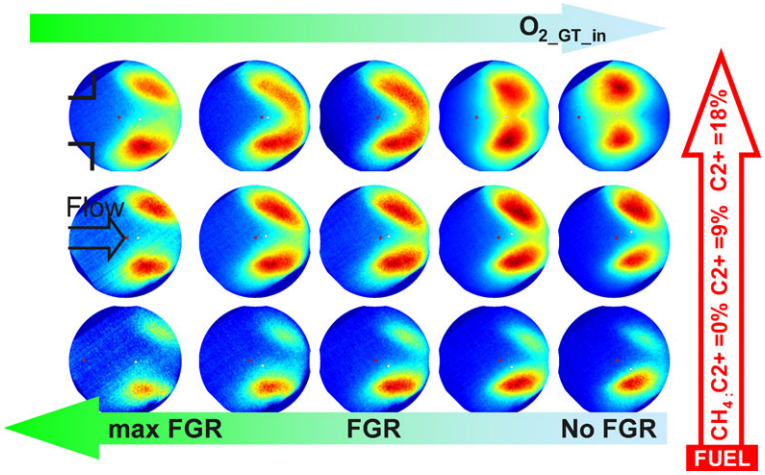

Fig. 13 SEV chemiluminescence images for varying FGR conditions and fuels (taken from [33])

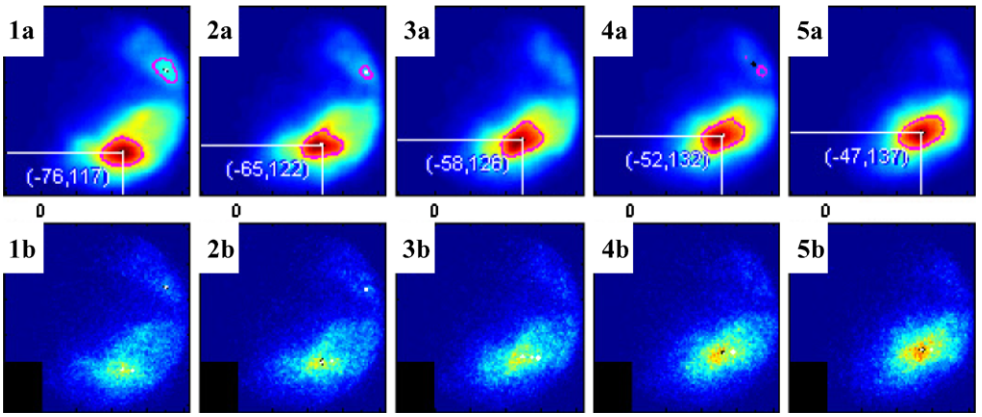

Fig. 14 Image sequences at full pressure conditions of five consecutive frames showing: (*top row*) the contour averaging method employed on smoothed flame images, (*bottom row*) corresponding unsmoothed false colour images with overlaid burner mouth and kernel positions. The kernel location labels have the following format: (transverse distance from axial centreline, axial distance downstream of burner mouth plane)

2. A contour averaging method was applied to each of the upper and lower regions of each image to identify raw, potential kernels.
3. To improve tracking, identified kernels that are very close to each other (on the same image) are merged together with the average position taken as the true location of the single auto-ignition kernel. The drawback to this process is the potential of merging two distinct kernels, but this drawback was observed to be eclipsed during testing by the advantage of generally improved results—specifically the prevention of large, unified hot flame regions from being interpreted as multiple kernels.
4. Once kernel identification has been established, it is possible to track movement of kernels through the use of a metric defining one kernel as the ancestor or descendant of another. This metric is simply the distance between one kernel and its potential descendant in the subsequent image of the sequence. Only if the distance between kernels in consecutive images is acceptable are the kernels considered related. Such a string of 'related' kernels may be called a 'kernel group.' If no ancestor is found to exist for a certain kernel, it is an 'initial' kernel. The frequency of appearance of these initial kernels is of interest, as will be discussed in the following section.
5. To reduce the effect of noise, initial kernels with no descendants (i.e., single member 'kernel groups') are disregarded.

In Fig. 14 the tracking of a kernel (in the lower flame region) is shown through five consecutive frames. The movement of kernel position can be seen in the top row of images, showing a clear downstream progression as its axial position (the second number in the ordered pair) steadily increases with each frame (which are temporally separated by 0.1 ms). The top row of images in Fig. 14 shows this process, with contours coloured in magenta. Step 5 is exemplified from image 4a to 4b, in which the single member kernel group identified is discarded as noise in a more refined stage of tracking shown by the bottom row of frames.

The following discussion relates to Fig. 15, which displays the axial positions of tracked kernels in a short period of time for a sample measurement point. For good kernel tracking it is important to determine the frequency of appearance of hot kernels. It is not sufficient to only identify the events of their first appearance in any sequence of images but good kernel tracking is also necessary to determine advection speed with sufficient accuracy. This is the case for kernel groups labelled A, D, I, K and L in Fig. 15.

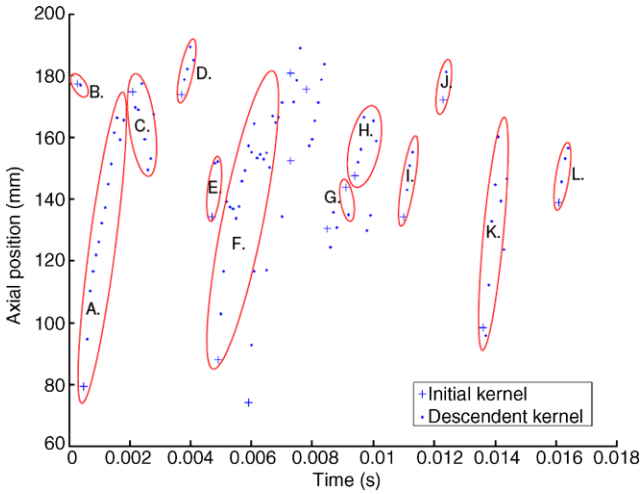

Fig. 15 Diagram of axial positions for tracked kernels in the lower flame vs. time. The plus symbols (+) denote initial kernels and the *dots* denote descendants. A selection of kernel groups are each labelled and circled in *red*. Only 0.018 s (corresponding to 180 images) of a sample series are shown here for demonstrative purposes

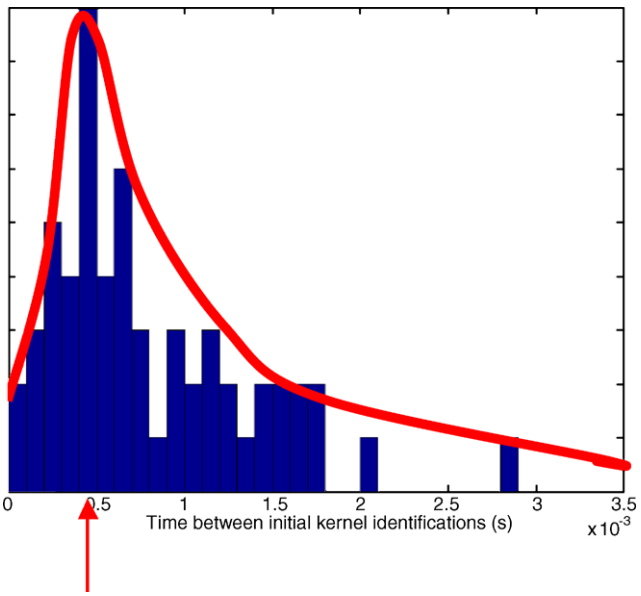

Fig. 16 Histograms of times between flame kernel appearances. The *red line* is manually added and estimates a probability density function (pdf)

Several factors contribute to recording misleading advection speeds. When a single kernel is 'lost' during its path downstream due to its brightness falling below the threshold intensity, and is then 'found' again at later time, the number of kernels measured at a certain speed is theoretically doubled. Examples of this are the pairs of kernel groups (G, H) and, conjecturally, (I, J). Unusually high advection speeds (many times the bulk flow speed) can also be attributed to erroneous tracking, whereby small kernel groups do not provide a longer-term average of motion.

Kernel advection speeds are calculated for each kernel group based on the distance between the most upstream and downstream tracked positions among the kernel group members, and the time between these occurrences. Thus, speeds highly depend on the quality of kernel tracking. Furthermore, speeds calculated to be negative are assigned to zero. This usually happens due to poor tracking and errors in the matching of ancestor kernels to their descendants.

Statistical analysis can be performed over a large data set. Probability density functions of Kernel advection velocity and frequency can then be derived as shown in Fig. 16. Poor kernel tracking is likely to result in a very flawed or skewed advection speed histogram (especially for flames with large kernels which are difficult to precisely locate). All kernels, which appear to move upstream are set to a speed of zero. This occurs for groups B, C and G in Fig. 15. While overall statistics is not sufficient for further modelling, the data in Fig. 16 clearly reveal a maximum probability for ignition times to occur.

The analysis has been conducted over a wide range of operating conditions and the conclusions drawn are as follows.

The ignition kernel appearance frequency increases when the sequential combustor inlet temperature rises, leading to an increase of the local chemical formation rate as the fuel mass flow rate is kept constant.

The ignition kernels are advected downstream along the mixing layer between hot gas recirculating in the reheat combustion chamber and the main flow. The ignition kernels are advected at the bulk flow velocity, which increases when increasing the inlet temperature. A link of these frequencies to the occurrence of combustion instabilities is currently only speculative but when resonance conditions are met such instabilities could be significant.

5.3 Phase locked spatial distributions

The impact of flame position on pulsation and emission behaviour based on chemiluminescence imaging has been described several times before for conventional premix burners [39]. The flame position normally depends on operating conditions like T_{flame} and burner velocity. To visualise the pulsation behaviour and link this to the design of the burner as well as to validate the design tools, phase resolved detection is used allowing detection of flame positions and shapes also as function of the pulsation phase angle (for given frequency). There are in principle two ways to record this phase matched data: by online signal processing [39], fast processing and direct phase angle determination or by free running image recording parallel to the recording of the pressure signal and phase matching the data in a post-processing step [40]. The latter method allows for a much higher flexibility and robustness like the sorting for more than one frequency within one sample. Since the set up is fairly simple the data acquisition can be done in standard image recording mode

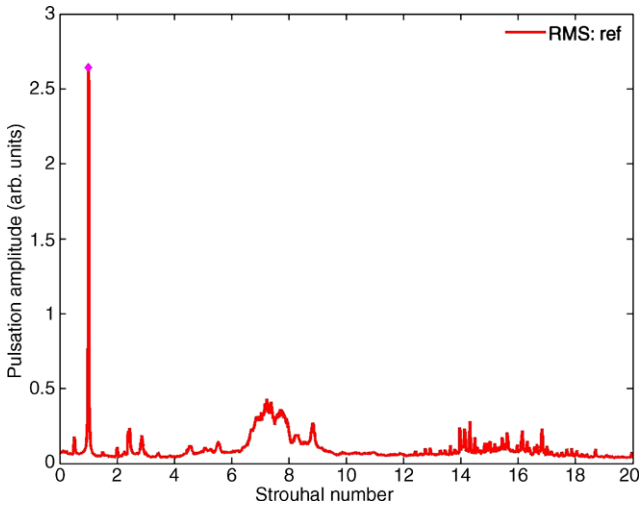

Fig. 17 SEV pulsation amplitudes plotted vs. frequency as Strouhal number

and analysis can be performed for cases of interest if required.

This method has been used for the SEV burner at high pressure conditions to study the first thermo-acoustic mode, which lies in this case around at a frequency of Strouhal ∼1 as shown in Fig. 17. The frequencies on the y-axis is expressed as the non-dimensional Strouhal number $\mathrm{Sr} = \mathrm{fq} \cdot D/u_{\mathrm{burner}}$ (with fq = frequency, D = burner diameter and u_{burner} = burner velocity).

Thermo-acoustic coupling in gas turbine combustion chamber is a well-known phenomenon. When the Rayleigh criterion [41] is satisfied, the fluctuating component of the heat release rate produced by the flame constructively interacts with the acoustic pressure. In that case a self-induced exponential amplification of the acoustic energy results. This acoustic amplitude growth is limited by nonlinear mechanisms defining a limit cycle. Most of the investigations that can be found in the existing literature cover the case of constructive interaction between flames and combustor acoustics for which the compact flame approximation is valid, i.e. the acoustic wavelength is large compared to the flame size. An example is given in Figs. 17 and 18 where the acoustic spectrum and chemiluminescence phase locked reconstruction over one oscillation cycle are shown. Note that this thermo-acoustic limit cycle is established at the dominant frequency visible in the acoustic spectrum in Fig. 17.

5.3.1 Short wavelength thermo-acoustic coupling

There are however some situations for which the compact flame assumption does not hold and they are much less documented. In such a case, the feedback mechanism involves acoustic eigenmodes featuring wavelengths of the order of reaction zone and are referred to in this paper as short wavelength thermo-acoustic coupling.

By considering the wavelength associated to this Strouhal number together with the chamber geometry, it can be concluded that the shown mode is axial with a dominant modulation of the overall intensity as seen in Fig. 18. The axial movement is less pronounced, but can be observed when comparing 90° and 270° images.

For the first mode this observation is in line with expectations. Higher modes are expected to exhibit several nodal planes resulting in smaller structures Mode shape visualisation and analysis of such higher modes by methods like the described phase matching method can be conducted but sufficient data quality and information about the pulsation mode shapes can only be gained from an optimised view angle. This is more demanding than for the axial mode. Such pulsations are also difficult to produce in a controlled manner, which makes the experiment difficult to conduct. This is the topic of the following section, where the objective is to characterise the coherent flame dynamics when it is submitted to a harmonic acoustic excitation where the acoustic wavelength is twice the flame size.

5.3.2 Atmospheric testing of "non-compact" flames

This study has been carried out at atmospheric conditions for which the test rig can be equipped with large optical access and advanced instrumentation which would be much more challenging at high pressure conditions. These experiments are carried out for the particular case of the turbulent auto-ignition flame (SEV) running with natural gas at atmospheric conditions. The aim is to get a better understanding of the key mechanisms that yield high amplitude oscillations of the acoustic pressure for non-compact flames with respect to the acoustic wavelength. One of the key mechanisms involved in the feedback loop responsible of the coupling is the flame response to acoustic perturbation. It is therefore important to conduct forced flow experiments with acoustic drivers used to excite the flame in order to extract its dynamic response.

The flame images were recorded by the same method as described with an intensified camera at 40 Hz before for the high-pressure rig together with analogue acoustic pressure signals at different location on the chamber walls. Phase locked averaging of the flame images was applied to extract the coherent component of the fluctuating heat release induced by the acoustic/combustion interaction. The camera view angle is comparable to that in Fig. 11. Four instantaneous snapshots of the auto-ignition flame are presented in Fig. 19.

In parallel, light from the flame is collected by a lens and filtered (DUX11) photomultiplier signals are recorded at 24 kHz. A lens was chosen such that the view angle is narrow to have some spatial resolution from specific zones of the flame, combined with high temporal resolution.

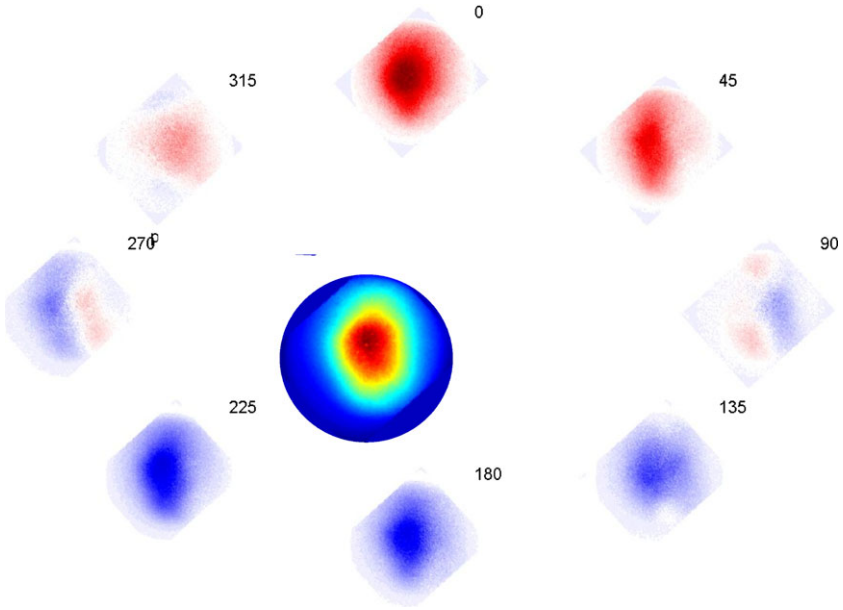

Fig. 18 Phase matched SEV chemiluminescence at full pressure conditions sorted after phase angle. Plotted in *red* are regions with positive deviation with respect to the average image (shown in the centre in usual colour map)

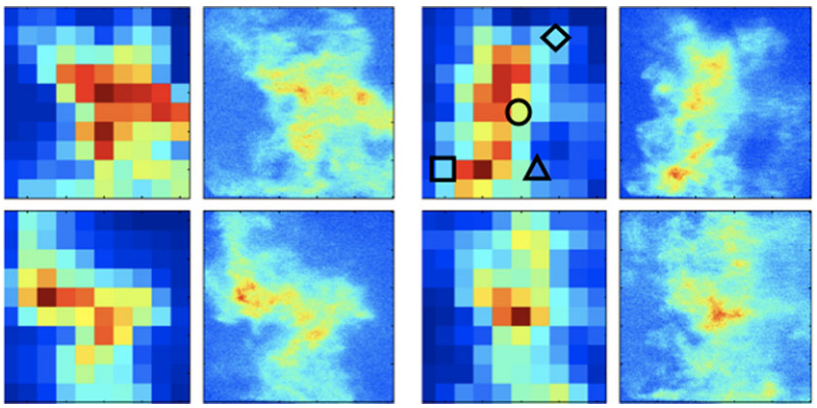

Fig. 19 Four flame snapshots randomly recorded together with their corresponding spatial averaging which is used to analyse coherent flame dynamics hidden behind the temperature driven turbulent auto-ignition process

Three microphones are mounted on the second side-wall of the combustion chamber in order to record acoustic pressure signals. The first transverse acoustic eigenmode of the combustion chamber is forced by means of two compression drivers (acting as loudspeakers) mounted on the combustion chamber walls (top–down out of phase excitation). The acoustic wavelength is twice the chamber height and the acoustic forcing amplitude is rather high. During the experiments, analogue signals and flame images are recorded simultaneously. The analogue signals are: the excitation signal feeding the speakers, the trigger signal providing the time at which pictures are taken, the light intensity signal (photomultiplier) and the pressure signals from the microphones.

The light intensity signal collected with the photomultiplier is first considered. During the test, the FFT was monitored to check whether the flame was responding or not to the acoustic excitation in terms of light intensity (assumed to be an indicator of the heat release). The photomultiplier was directed toward different flame zones, and the online monitoring of the spectrum indicated that certain flame zones were responding, whereas others were not, which is crucial information and which will be discussed further in the following. The signal analysed corresponds to a photomultiplier lens pointing at a flame zone. As illustrated in Fig. 20 a clear peak at the excitation frequency is present in the spectrum.

Figure 20 reveals that the flame does respond to the short wavelength acoustic excitation. The coherent component of the chemiluminescence (at the acoustic excitation frequency) has a small amplitude with respect to the signal standard deviation, i.e. the signal to noise ratio is poor. Although a clear peak is visible in the spectrum the energy contained at this frequency is small compared to the one present in the low frequency range.

In contrast with this photomultiplier analogue signal, the images are collected at a low rate, which is far below the oscillation frequency. This is why phase locked averaging (PLA) was considered to process the collected images, and to extract the dynamic component of the heat release induced by the harmonic acoustic excitation.

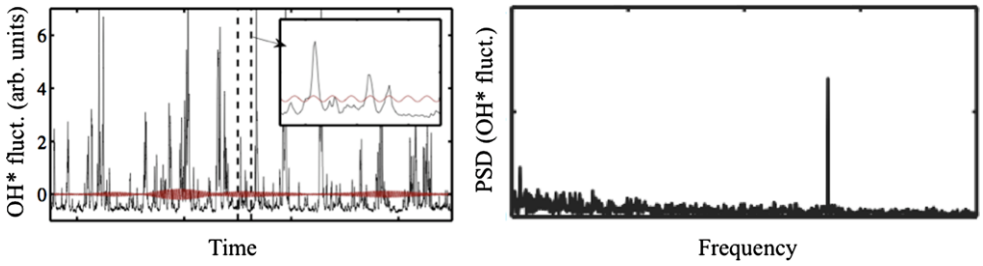

Fig. 20 *Left*: Raw fluctuating signal recorded with the photomultiplier (*black*) together with its narrow-band filtered component around the excitation frequency (*red*). The corresponding acoustic wavelength is approximately twice the flame height (see Fig. 19). *Right*: Fast Fourier Transform of the raw signal where the peak in the spectrum corresponds to the excitation frequency

Standard PLA of images of acoustically driven flames is known to yield useful results and allows one to nicely decompose coherent flame dynamics over an oscillation cycle as shown in the first part of the section (see Fig. 18). However, it is also known that the amount of collected data influences the results.

At a given location the signal features a standard deviation near 1 (over almost one minute) Considering a sample of this size and applying phase averaging to this sample, it is important to estimate the minimum sample size required to get an acceptable estimation of the coherent component of the signal. From the filtered signal we know that the coherent component features an amplitude of $|I'c| = 0.06$.

To get a 70 % confidence interval for the phase averaged chemiluminescence twice smaller than the harmonic component the size of samples per phase angle required is approximately 1000. This value is relatively high because the ratio between coherent response and low frequencies content is relatively poor for the turbulent auto-ignition flame forced with short wavelength acoustic tone as considered in this study.

The flame is not entirely responding to the excitation as was observed by scanning the combustion zone with the photomultiplier, simultaneously monitoring the light intensity spectrum and tracking the presence and the amplitude of a peak at the excitation frequency. Since the zones vary in their response amplitude the 1000 samples/phase-angle constrain is not valid for all of the flame regions, especially before applying the PLA method to flame images: At each pixel, an average value per phase angle can be computed, but this value can be far from the actual average value depending on the sample size. Before applying PLA to a set of 10000 recorded images, it was decided to perform a spatial averaging in order to mimic the use of the narrow view-angle photomultiplier and get similar spatially integrated data. In Fig. 19, four flame snapshots are presented together with their corresponding resized images to illustrate this first step of the processing.

Using trigger signals that define the time at which images are recorded together with the excitation signal, each flame snapshot is assigned to its corresponding acoustic forcing phase angle. Images are then sorted in increasing phase angle and harmonic decomposition for each of the 100 spatially average zones (see Fig. 19) in order to get the corresponding Fourier coefficients.

Example of results for different zones is given in Fig. 21. The corresponding zones are indicated in one of the snapshots in Fig. 19. In contrast to the “square”, “triangle” and “diamond” zones, it is not possible to state if the extracted harmonic response is meaningful for the “circle” zone, since the oscillation amplitude is lower than the standard error. Therefore a confidence factor is introduced in order to quantify the quality of the result. This factor is the ratio between the harmonic amplitude deduced from the processing and the standard error.

The entire set of zones is processed as described previously and results are presented in Fig. 22 showing the significant difference to the flame snapshots from Fig. 19. This is due to the turbulence level being higher and yields standard deviations of the light intensity signal (assumed proportional to the heat release) of the order of the mean values. From the confidence factor map shown in Fig. 22, one can see that four regions feature a good confidence factor, meaning that one can be confident with the processing and that the harmonic component extracted in these regions are reliable evaluations of the heat release rate response at the excitation frequency. The amplitude plot shows three regions to respond with a high amplitude, and these regions can be roughly superimposed to high confidence index regions. The phase pattern indicates that the acoustics drives the coherent heat release fluctuation in a rather complex way: an out of phase oscillation between the upper and lower parts of the flame is combined to an advection process.

6 Conclusions

A wide range of chemiluminescence applications used for the combustor development are covered in this overview. Flame spectra and photomultiplier signals are used for flame

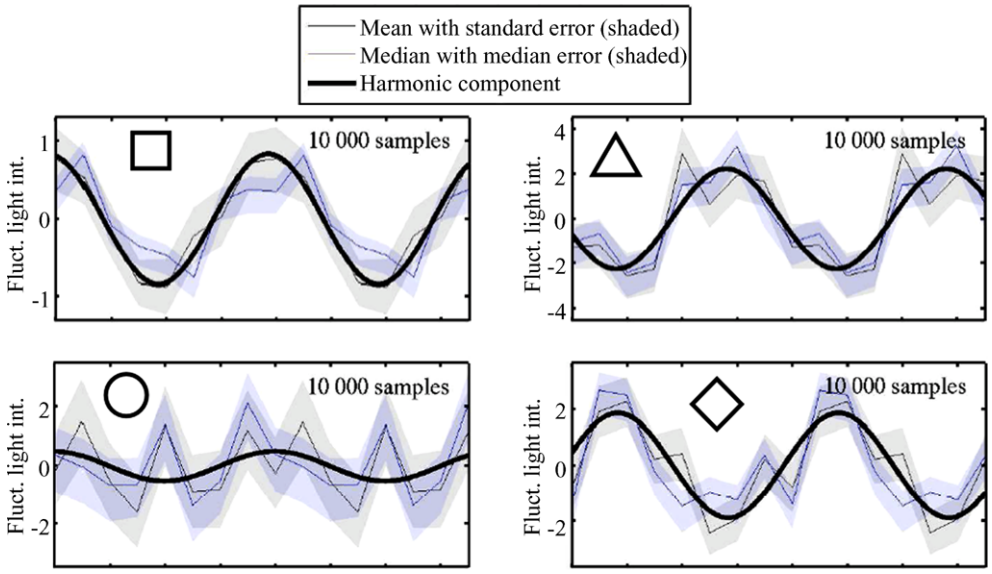

Fig. 21 PLA result for different groups of pixels indicated by a *square*, a *triangle*, a *circle* and a *diamond* in Fig. 1 (x-axis: phase angle for two acoustic periods $\sim 4\pi$ where $t = 1/f_{\text{excitation}}$). For each zone, 10 000 values of the signal were used to perform the averaging. For each value, the phase angle is deduced from the excitation signal, which is taken as reference. Mean and median averages are presented, together with the mean and median standard error (*shaded zones*). The *thick black line* is the harmonic component computed from the mean averages

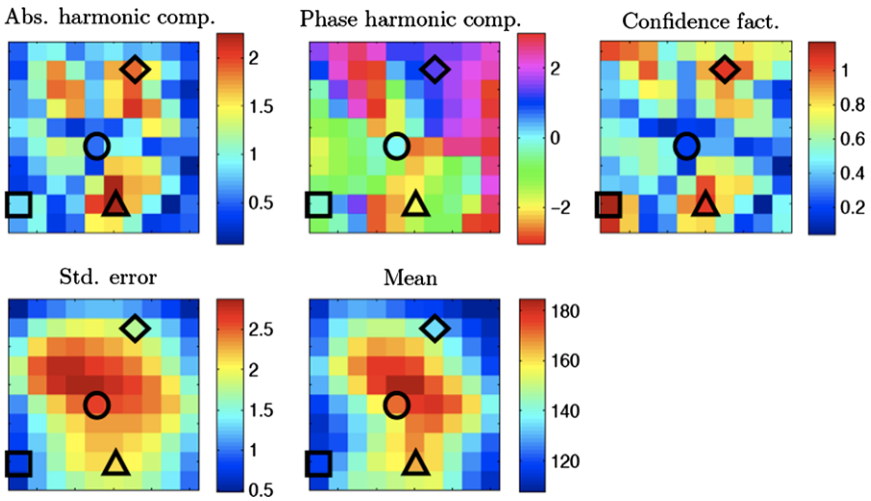

Fig. 22 Results obtained from combined spatial averaging and PLA method. *Top*: Amplitude and phase of the extracted harmonic component of the fluctuating chemiluminescence, together with the confidence factor associated with this computation. *Bottom*: Standard error associated with the PLA of the individual zones and mean OH* chemiluminescence

sensing and monitoring purposes as well as flame transfer function measurements. The best strategy to minimise NO_x formation might require several different detection bands. The method would benefit from a better understanding of the broad background emission dominating the chemiluminescence spectrum of the gas turbine flame. Also the formation pathways and the occurrence of excited states are not finally clarified with respect to their molecular dynamics. The good experience in terms of NO_x-reduction in field engines with the commercial flame sensing system for premix annular combustors are the motivation to further intensify the development effort for flame sensing basics, in order to better understand the interesting physics and chemistry of the process, as this might be crucial for the improvement of the sensing method in terms of robustness and application range and might give important insights in the combustion chemistry modelling. Such improved understanding would possibly also extend the range of application of the existing GT flame sensing available for Alstom's annular combustion systems also to reheat combustion or flue gas recirculation.

Flame imaging under realistic gas turbine conditions supports the combustor research and development for the optimisation of stability and emissions by several methods. Averaged images allow one to investigate stable operating conditions, while time dependent detection yields insights in acoustic mode shapes which are required for the development of stable combustors. High speed imaging is useful to explore active combustion mechanisms as demonstrated for a sequential combustion system.

Sophisticated data processing was able to show that SEV flames respond to the short wavelength acoustic excitation and that the flame response is spatially distributed and features complex dynamics combining an out of phase coherent auto-ignition between top and bottom regions of the reaction zone together with an advection process. Unlike in conventional premix combustors, in the sequential combus-

tor the coherent component of the heat release rate (driven by the acoustics) is weak compared to the non-coherent one (induced by the turbulent auto-ignition process) despite the strength of the acoustic excitation.

Acknowledgements The authors acknowledge Lawrence Byerley and Marissa Browers for their helpful contributions and the company LaVision for technical support developing the ICCD cameras.

References

1. C. Steinbach, N. Ulibarri, M. Garay, H. Lübcke, T. Meeuwissen, K. Haffner, J. Aubry, D. Kodim, ASME Turbo Expo, GT2006-90943, 2006
2. M. Lauer, T. Sattelmayer, J. Eng. Gas Turbines Power **132**, 061502 (2010)
3. M. Lauer, M. Zellhuber, C. Aul, T. Sattelmayer, ASME Turbo Expo, 45105, 2011
4. M. Lauer, T. Sattelmayer, Appl. Phys. B (2012, in press)
5. A.G. Gaydon, *The Spectroscopy of Flames* (Chapman and Hall, London, 1957)
6. E. Mancaruso, B.M. Vaglieco, Fuel **90**, 511 (2011)
7. T. Kathrotia, M. Fikri, M. Bozkurt, M. Hartmann, U. Riedel, C. Schulz, Combust. Flame **157**, 1261 (2010)
8. C.S. Panoutsos, Y. Hardalupas, A.M.K.P. Taylor, Combust. Flame **156**, 273 (2009)
9. J.M. Hall, E.L. Petersen, Int. J. Chem. Kinet. **38**, 714 (2006)
10. V.N. Nori, J.M. Seitzman, AIAA-2007-0466, 2007
11. Y.B. Zeldovich, Acta Physiochim. USSR **21**, 577 (1946)
12. F. Biagioli, F. Guethe, Combust. Flame **151**, 274 (2007)
13. D.G. Nicol, Trans. Am. Soc. Mech. Eng. **117**, 100 (1992)
14. P.C. Malte, D.T. Pratt, in *Proceedings of the 15th Symposium on Combustion*, The Combustion Institute (1974), p. 1061
15. J.W. Bozzelli, M. Anthony, Int. J. Chem. Kinet. **27**, 1097 (1995)
16. C.P. Fenimore, in *Proceedings of the 13th Combustion Symposium*, The Combustion Institute (1971), p. 373
17. E. Petersen, M. Knopp, N. Donato, F. Guethe, J. Eng. Gas Turbines Power **134**, 051501 (2012)
18. J.-M. Samaniegoa, F.N. Egolfopoulos, T. Bowman, Combust. Sci. Technol. 183 (1995)
19. A. Bergeat, T. Calvo, F. Caralp, J.H. Fillion, G. Dorthe, J.C. Loison, Faraday Discuss. **119**, 67 (2001)
20. S.A. Carl, H.M.T. Nguyen, R.M.I. Elsamra, M.T. Nguyen, J.J. Peeters, Chem. Phys. **122**, 114307 (2005)
21. R.M.I. Elsamra, S. Vranckx, S.A. Carl, J. Phys. Chem. A **109**, 10287 (2005)
22. Y. Hardalupas, M. Orain, Combust. Flame **139**, 188 (2004)
23. T. Yamaguchi, K.T.V. Grattan, H. Uchiyama, T. Yamada, Rev. Sci. Instrum. **68**, 197 (1997)
24. J. Kojima, Y. Ikeda, T. Nakajima, in *36th AIAA/ASME/SAE/ASEE Joint Propulsion Conference and Exhibit AIAA-3394* (2000)
25. V. Nori, J. Seitzman, AIAA Paper No. AIAA-2007–466, 2007
26. D. Guyot, F. Guethe, B. Schuermans, ASME Turbo Expo, GT2010-23135, 2010
27. B. Higgins, M. McQuay, F. Lacas, J. Rolon, N. Darabiha, S. Candel, Fuel **80**, 67 (2001)
28. B. Higgins, M. McQuay, F. Lacas, S. Candel, Fuel **80**, 1583 (2001)
29. S.M. Correa, Combust. Sci. Technol. **87**, 329 (1993)
30. M. Kopp, N. Donato, M. Brower, E. Petersen, F. Guethe, Appl. Phys. B (2012, in press)
31. F. Guethe, J. Hellat, P. Flohr, J. Eng. Gas Turbines Power **131**, 021503 (2009)
32. B. Schuermans, F. Guethe, D. Guyot, D. Pennel, O.C. Paschereit, J. Eng. Gas Turbines Power **132**, 111503 (2010)
33. F. Guethe, D. Stankovic, F. Genin, K. Syed, D. Winkler, ASME Turbo Expo, GT2011-45379, 2011
34. A. Seipel, A. Brockhinke, K. Kohse-Hoinghaus, in *2nd International Workshop on Chemiluminescence and Heat Release*, München (2009)
35. D. Guyot, C.O. Paschereit, in *Proc. of the 45th AIAA/ASME/SAE/ASEE Joint Propulsion Conference, AIAA-2009-5413* (2009)
36. A. Ciani, A. Eroglu, F. Guethe, B. Paikert, ASME Turbo Expo, GT2010-22891, 2010
37. E. Mastorakos, Prog. Energy Combust. Sci. **35**, 57 (2009)
38. A. Koch, C. Naumann, W. Meier, M. Aigner, ASME Turbo Expo GT-2005-68405, 2005
39. F. Guethe, R. Lachner, B. Schuermans, F. Biagioli, W. Geng, A. Inauen, S. Schenker, R. Bombach, W. Hubschmidt, in *44th AIAA Aerospace Sciences Meeting and Exhibit* (2006)
40. F. Guethe, B. Schuermans, Meas. Sci. Technol. **18**, 3036 (2007)
41. J.W.S. Rayleigh, Nature **18**, 319 (1878)